

can momentarily produce a single-crack state. As explained in ref. 13, the high peaks in the velocity measurements correspond to these single-crack states, because, when several cracks are propagating simultaneously, the available energy is distributed between them, and the front velocity drops. Thus beyond v_c there are moments when we measure the velocity of a single crack moving in a known energy density.

An important prediction of equation (2) is that a crack, having no 'inertia', will immediately jump to its predicted velocity. Another prediction of linear elastic theory¹², verified in PMMA¹⁸, is that upon a sudden change in loading, the stress field will assume its asymptotic value within the time needed for a shear wave to pass. Thus, $\sim 1 \mu\text{s}$ after the 'death' of a side branch of length 1 mm, the stress field throughout the singular zone will be that of a single crack. As above 450 m s^{-1} , the system becomes effectively two-dimensional (ref. 2), the highest peaks of the instantaneous velocity should then be described by equation (2); alternatively, we can use equation (1) to derive the value of Γ for a single crack moving at the peak velocities. We check this premise by comparing these derived values with the measurements of Γ in a strip^{2,14}. These measurements showed that above v_c , when the total fracture surface formed by both the main crack and its branches was taken into account, Γ (per unit fracture surface) has the constant value of $0.9\Gamma(v_c)$. Comparison between the measured and derived values of Γ was performed using the peak velocities obtained in a number of experiments that were conducted under widely diverse conditions. The results (Fig. 3a) indicate that the theory works remarkably well. As in ref. 14, the derived values of $\Gamma(v)$ were constant and equal to $0.9\Gamma(v_c)$. The 10% drop in Γ relative to $\Gamma(v_c)$ may result from the extremely high acceleration rate preceding the peak velocities. This effect also appears at fracture initiation in PMMA, when at comparable acceleration rates, an overshoot of the initial crack velocity, consistent with an effective 10% reduction in Γ , is observed.

In Fig. 3b, c we directly compare the instantaneous velocity measurements of a number of different cracks with the corresponding velocity curves predicted by equation (2). In all of the data sets the theoretical curve was calculated (with no adjustable parameters) using a single value of $\Gamma(v) \approx 0.9\Gamma(v_c)$ ($= 3,000 \text{ J m}^{-2}$ in PMMA). Above v_c , all of the highest-velocity peaks are accurately described by the theoretical curve, despite the wide variations in experimental conditions. At the highest energy fluxes, peak velocities, correctly described by equation (2), indeed exist in excess of $0.9v_R$. Thus to see the approach to v_R , one need only look at the instantaneous velocity of single-crack states. These results are consistent with both calculations⁸ and experiments¹⁹ in which the micro-branching instability was artificially suppressed. □

Methods

The experiments were conducted in thin, quasi-two-dimensional cast PMMA and soda lime glass sheets of size $380 \times 440 \text{ mm}$ in the x (propagation) and y (loading) directions, and thickness 2 and 3 mm, respectively. All samples were loaded by uniform displacement of the vertical boundaries. Fracture was initiated at the tip of a small notch inserted midway between the vertical boundaries at the sample's edge. The initial length and tip curvature of this notch determined the amount of elastic energy stored in the sample before the onset of fracture. The crack velocity was measured by the technique described in ref. 2 with the addition of analogue differentiation of the signal before its digitization. A velocity resolution of better than 10 m s^{-1} in PMMA and of the order of 50 m s^{-1} in glass was attained. All the data presented were measured before the arrival of reflected stress waves from the far boundaries of the plates. Reflected waves from the sample edge behind the initial crack, as in ref. 20, had no noticeable effect on the crack. Thus the loading conditions were, effectively, those of constant stress loading. As this can be mapped to constant loading of the crack faces, the experiments are compatible with the assumptions leading to equation (1). $G(I)$ was computed numerically for the precise geometry of the plates we used. The values of v_R , obtained by a direct measurement, are 930 m s^{-1} (PMMA) and $3,300 \text{ m s}^{-1}$ (glass).

Received 9 July; accepted 5 October 1998.

1. Bergkvist, H. Some experiments on crack motion and arrest in polymethylmethacrylate. *Eng. Fracture Mech.* **6**, 621–626 (1974).
2. Sharon, E. & Fineberg, J. Microbranching instability and the dynamic fracture of brittle materials. *Phys. Rev. B* **54**, 7128–7139 (1996).
3. Ravi-Chandar, K. & Knauss, W. G. An experimental investigation into dynamic fracture. III. On steady-state crack propagation and crack branching. *Int. J. Fracture* **26**, 141–154 (1984).
4. Ravi-Chandar, K. & Knauss, W. G. An experimental investigation into dynamic fracture. II. Microstructural aspects. *Int. J. Fracture* **26**, 65–80 (1984).
5. Fineberg, J., Gross, S. P., Marder, M. & Swinney, H. L. Instability in the propagation of fast cracks. *Phys. Rev. B* **45**, 5146–5154 (1992).
6. Marder, M. & Liu, X. M. Instability in lattice fracture. *Phys. Rev. Lett.* **71**, 2417–2424 (1993).
7. Marder, M. & Gross, S. P. Origin of crack tip instabilities. *J. Mech. Phys. Solids* **43**, 1–48 (1995).
8. Xu, X. P. & Needleman, A. Numerical simulations of fast crack growth in brittle solids. *J. Mech. Phys. Solids* **42**, 1397–1437 (1994).
9. Johnson, E. Process region changes for rapidly propagating cracks. *Int. J. Fracture* **55**, 47–63 (1992).
10. Lobkovsky, A. & Langer, J. S. Critical examination of cohesive-zone models in the theory of dynamic fracture. *J. Mech. Phys. Solids* **46**, 1521–1526 (1998).
11. Ching, E. S. C., Langer, J. S. & Nakanishi, H. Dynamic instabilities in fracture. *Phys. Rev. Lett.* **76**, 1087–1090 (1996).
12. Freund, L. B. *Dynamic Fracture Mechanics* (Cambridge Univ. Press, New York, 1990).
13. Sharon, E., Gross, S. P. & Fineberg, J. Local crack branching as a mechanism for instability in dynamic fracture. *Phys. Rev. Lett.* **74**, 5096–5099 (1995).
14. Sharon, E., Gross, S. P. & Fineberg, J. Energy dissipation in dynamic fracture. *Phys. Rev. Lett.* **76**, 2117–2120 (1996).
15. Boudet, J. F., Giliberto, S. & Steinberg, V. Dynamics of crack propagation in brittle materials. *J. Phys. II* **6**, 1493–1516 (1996).
16. Abraham, F. F., Brodbeck, D., Rafey, R. A. & Rudge, W. E. Instability dynamics of fracture—a computer simulation investigation. *Phys. Rev. Lett.* **73**, 272–275 (1994).
17. Zhou, S. J., Lomdahl, P. S., Thomson, R. & Holian, B. L. Dynamic crack processes via molecular dynamics. *Phys. Rev. Lett.* **76**, 2318–2321 (1996).
18. Vu, B. Q. & Kinra, V. K. Brittle fracture of plates in tension. Static field radiated by a suddenly stopping crack. *Eng. Fracture Mech.* **15**, 107–114 (1981).
19. Washabaugh, P. D. & Knauss, W. G. A reconciliation of dynamic crack velocity and rayleigh wave speed in isotropic brittle solids. *Int. J. Fracture* **65**, 97–114 (1994).
20. Morrissey, J. W. & Rice, J. R. Crack front waves. *J. Mech. Phys. Solids* **46**, 467–487 (1998).

Acknowledgements. We thank L. B. Freund for supplying us with finite-element calculations of $G(I)$. This work was supported by the US-Israel Binational Fund.

Correspondence and requests for materials should be addressed to J.F. (e-mail: jay@vms.huji.ac.il).

A controlled-release microchip

John T. Santini Jr*, Michael J. Cima† & Robert Langer*

* Department of Chemical Engineering, † Department of Materials Science and Engineering, Massachusetts Institute of Technology, Cambridge, Massachusetts 02139, USA

Much previous work in methods of achieving complex drug-release patterns has focused on pulsatile release from polymeric materials in response to specific stimuli¹, such as electric^{2–5} or magnetic^{6,7} fields, exposure to ultrasound^{7,8}, light⁹ or enzymes¹⁰, and changes in pH¹¹ or temperature^{12–14}. An alternative method for achieving pulsatile release involves using microfabrication technology to develop active devices that incorporate micro-metre-scale pumps, valves and flow channels to deliver liquid solutions^{15,16}. Here we report a solid-state silicon microchip that can provide controlled release of single or multiple chemical substances on demand. The release mechanism is based on the electrochemical dissolution of thin anode membranes covering microreservoirs filled with chemicals in solid, liquid or gel form. We have conducted proof-of-principle release studies with a prototype microchip using gold and saline solution as a model electrode material and release medium, and we have demonstrated controlled, pulsatile release of chemical substances with this device.

Controlled release from our microchip involves no moving parts. Release from a particular reservoir is initiated by applying an electric potential between the anode membrane covering that reservoir and a cathode. Fig. 1a shows a cut-away portion of a prototype microchip containing reservoirs filled with the chemical to be released. The devices used in this study were 17 mm by 17 mm by 310 μm and contained 34 reservoirs. Device size could be reduced to $< 2 \text{ mm}$, depending on the particular application. As a point of reference, a device of the size used in these studies (17 mm) has enough surface area to accommodate over 1,000 reservoirs.

Devices for this study were fabricated by a sequential process using silicon wafers and microelectronic processing techniques^{17,18} including ultraviolet photolithography, chemical vapour deposition (CVD), electron beam evaporation and reactive ion etching. Each device contained reservoirs that extended completely through the wafer. The reservoirs were square pyramidal in shape (that is, they contained one large and one small square opening, see Fig. 1b), had a volume of ~ 25 nl, and were sealed on the small square end ($50 \times 50 \mu\text{m}$) by a $0.3\text{-}\mu\text{m}$ -thick, gold membrane anode. Gold was chosen as a model membrane material because it is easily deposited and patterned, has a low reactivity with other substances and resists spontaneous corrosion in many solutions over the entire pH range. However, the presence of a small amount of chloride ion creates an electric potential region which favours the formation of soluble gold chloride complexes¹⁹. Holding the anode potential in this corrosion region enables reproducible gold dissolution. Potentials below this region are too low to cause appreciable corrosion, whereas potentials above this region result in gas evolution and formation of a passivating gold oxide layer that causes corrosion to slow or stop. Other metals such as copper or titanium tend to dissolve spontaneously under these conditions or do not form soluble materials on application of an electric potential. Although it is used as a model compound in these studies, gold has also been shown to be a biocompatible material²⁰.

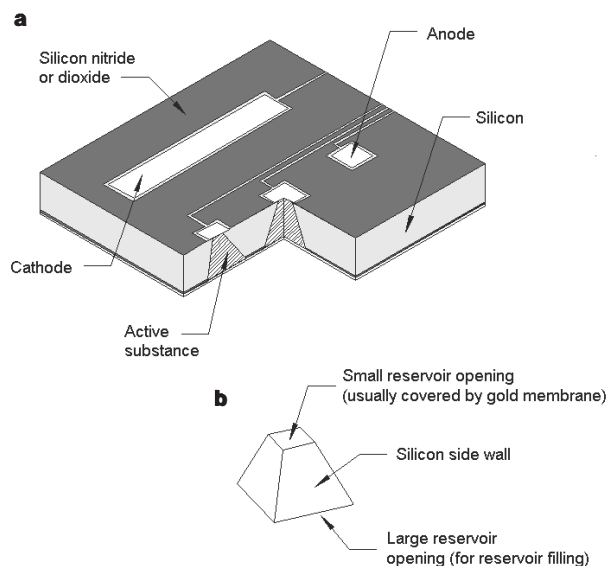


Figure 1 A prototype microchip for controlled release showing the shape of a single reservoir. **a**, Fabrication of these microchips began by depositing $\sim 0.12 \mu\text{m}$ of low stress, silicon-rich nitride on both sides of prime grade, (100) silicon wafers using a vertical tube reactor. The silicon nitride layer on one side of the wafer was patterned by photolithography and electron cyclotron resonance (ECR) enhanced reactive ion etching (RIE) to give a square device (17×17 mm) containing 34,480- μm -square reservoirs. The silicon nitride served as an etch mask for potassium hydroxide solution at 85°C , which anisotropically etched square pyramidal reservoirs (**b**) into the silicon along the (111) crystal planes until the silicon nitride film on the opposite side of the wafer was reached. The newly fabricated silicon nitride membranes completely covered the $40\text{--}60 \mu\text{m}$ square openings of the reservoir. Gold electrodes ($0.3 \mu\text{m}$ thick, with a $0.01\text{-}\mu\text{m}$ chromium adhesion layer) were deposited and patterned over the silicon nitride membranes by electron beam evaporation and lift-off. A $0.6\text{-}\mu\text{m}$ layer of plasma enhanced chemical vapour deposition silicon dioxide was deposited at 350°C over the entire electrode containing surface. The silicon dioxide located over portions of the anode, cathode and bonding pads were etched with ECR-enhanced RIE to expose the underlying gold film; this technique was then used to remove the thin silicon nitride and chromium membranes located in the reservoir underneath the gold anode.

Some portions of the electrodes must be protected from unwanted corrosion by an adherent, non-porous coating that isolates the electrode materials from the surrounding electrolyte. Silicon dioxide (SiO_2) was used as a model protective coating because its physical properties can be tailored to a particular application by selecting appropriate processing conditions. For example, SiO_2 deposited by CVD at low temperatures ($<100^\circ\text{C}$) tends to be porous and non-adherent in solution, whereas high-temperature ($>700^\circ\text{C}$) deposition or annealing results in denser SiO_2 but may also lead to thermal grooving and void formation in gold films²¹. We used plasma-enhanced CVD at moderate temperatures (350°C) to address these problems and produce SiO_2 films possessing adequate density and adhesion with negligible gold void formation. Light microscopy revealed no evidence of corrosion following the applied potential in those areas of the gold electrodes covered by SiO_2 , except in those regions immediately adjacent to the exposed gold membrane.

The gold membrane anodes of each microchip were examined for defects (such as pinholes) using reflected and transmission light microscopy after completion of the entire fabrication process. Reservoirs covered by defect-free, gold membrane anodes were considered viable for use in chemical-release experiments and were loaded with model chemical substances, sodium fluorescein and $^{45}\text{Ca}^{2+}$ (as CaCl_2), selected for ease of detection. Inkjet printing, in combination with a computer-controlled alignment apparatus²², is capable of depositing as little as 0.2 nl of a liquid or gel solution of known concentration into each reservoir. Microsyringe pumps also have the ability to deposit nanolitre quantities of solutions into device reservoirs. We found that these two filling methods work well and prevent any leaking of solutions or gels, such as our aqueous solutions composed of 15–25% (by volume) liquid polymer (polyethylene glycol, relative molecular mass $M_r = 200$) and the model release compounds. The water quickly evaporates after injection leaving only liquid polymer and model compound in the reservoir. The reservoirs are then covered with squares of a thin adhesive plastic and sealed with a waterproof epoxy. The gold membranes do not appear to be fragile even though the liquid material in a filled reservoir can exert a stress on the gold membrane anode due to capillary forces. Calculations indicate that these capillary forces are nearly two orders of magnitude smaller than that required to rupture a $0.3\text{-}\mu\text{m}$ -thick gold membrane, which can withstand pressures up to 3 lb in^{-2} . In addition, prototype devices have been stored for over a year without any known effects on operation or reliability.

The objective of initial release experiments was to determine if pulsatile release of a single compound could be obtained from a microchip device. Release was achieved from a reservoir of a prototype device immersed in phosphate-buffered saline (PBS) by applying a potential of $+1.04$ volts with respect to a saturated

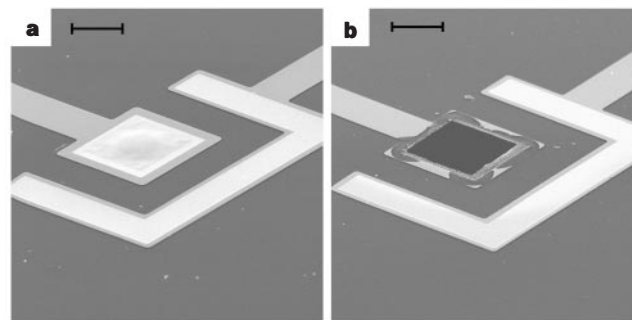


Figure 2 Removal of an anode membrane to initiate release from a reservoir. **a, b**, Scanning electron micrographs of a gold membrane anode covering a reservoir are shown before (**a**) and after (**b**) the application of $+1.04$ V w.r.t. SCE for several seconds in PBS. (Scale bar, $50 \mu\text{m}$.)

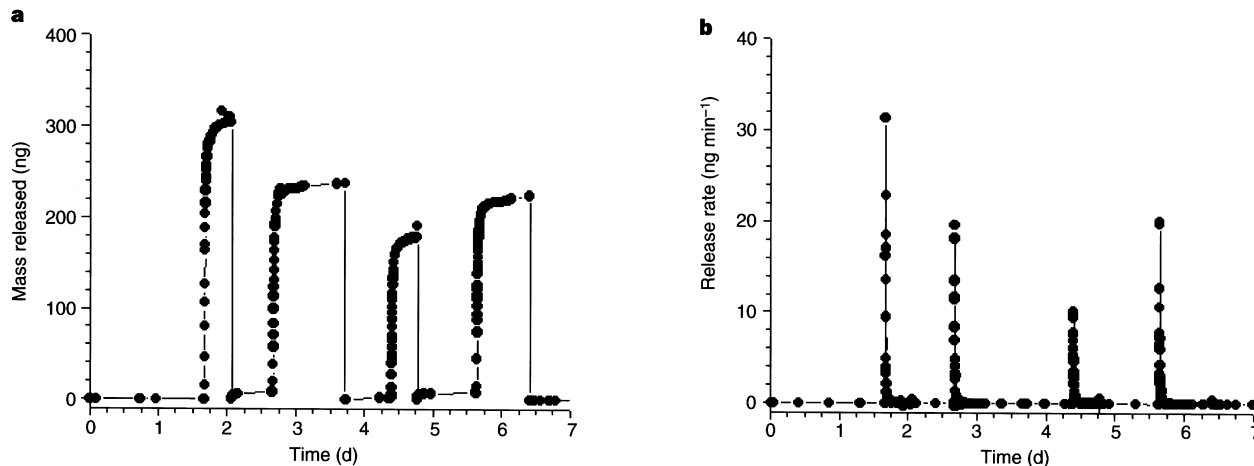


Figure 3 Pulsatile release of a single substance from a microchip device. **a**, The total mass of sodium fluorescein released into PBS over a period of several days is shown for each of four reservoirs. This release study was conducted in PBS stirred with a magnetic stirring bar at room temperature. The device was submerged in the PBS for >36 h before the first release to ensure that there was no leakage from any of the loaded reservoirs. The tip of the SCE was placed within 1–3 mm of the anode surface immediately before application of the electric potential. Release of fluorescein was obtained on demand by applying a potential of +1.04 V w.r.t. SCE for up to 30 s to each anode. The SCE was removed

immediately after the potential was applied. Samples (3 ml) were taken every few minutes from the release medium, analysed for dye content in a fluorimeter, and replaced with an equal volume of fresh PBS solution. The entire release medium (100 ml) was replaced with fresh solution several hours after each release. The release rate for the same experiment is shown in **b**. The release rate was calculated by taking the amount of fluorescein released between two time points and dividing it by the time elapsed, starting after the device was immersed in the PBS.

calomel reference electrode (+1.04 V w.r.t. SCE) to the gold anode covering that reservoir. The use of a reference electrode ensured that the potential of the gold membrane anode remained in the gold corrosion region during activation. Figures 2a and b show a gold membrane anode before and after a potential was applied in PBS. Release of the fluorescent model compound, sodium fluorescein, from a reservoir was detected by fluorescence spectroscopy within 1–2 minutes after the potential was applied (Fig. 3).

Subsequent release experiments were designed to determine if the independent release of multiple compounds could be obtained from a single device. Reservoirs containing one of two model compounds

were opened by applying +1.04 V w.r.t. SCE to the corresponding anode immersed in saline solution without phosphate buffer. The pulsatile release of $^{45}\text{Ca}^{2+}$ ions and sodium fluorescein over a period of several hours was achieved, showing that multiple compounds can be released independently from a single microchip device (Fig. 4).

The release studies demonstrate that the activation of each reservoir can be controlled individually, creating a possibility for achieving many complex release patterns. Varying amounts of chemical substances in solid, liquid or gel form can be released into solution in either a pulsatile manner, a continuous manner, or a combination of both, either sequentially or simultaneously from a single device. Such a device has additional potential advantages including small size, quick response times and low power consumption. In addition, all chemical substances to be released are stored in the reservoirs of the microchip itself, creating a possibility for the future development of autonomous devices. A microbattery, multiplexing circuitry and memory could be integrated directly onto the device, allowing the entire device to be mounted onto the tip of a small probe, implanted, swallowed, integrated with microfluidic components to develop a 'laboratory-on-a-chip', or incorporated into a standard electronic package, depending on the particular application. Some fields where this device may become useful include medical diagnostics, analytical chemistry, chemical detection, industrial process monitoring and control, combinatorial chemistry and microbiology. Future work will focus on improving reservoir filling methods and determining the factors that control the release of material from opened reservoirs. Gold and silicon were used as model materials for the prototype device in these proof-of-principle release studies. In the future, proper selection of biocompatible device materials may result in the development of an autonomous, controlled-release implant ('pharmacy-on-a-chip') or a highly controllable tablet ('smart tablet') for drug delivery applications. □

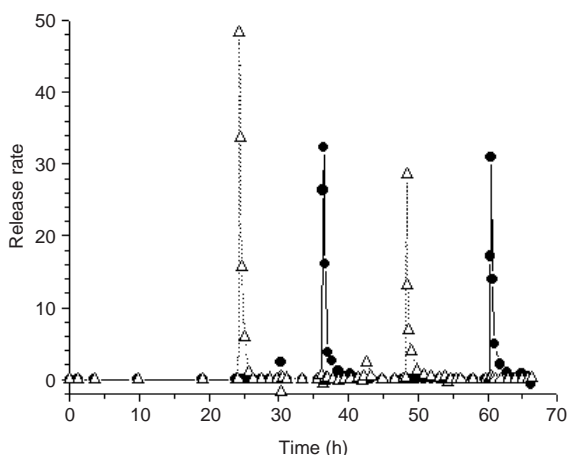


Figure 4 Pulsatile release of multiple substances from a single microchip device. The release rate of $^{45}\text{Ca}^{2+}$ ions (open triangles; vertical scale in units of $5 \times \text{nCi min}^{-1}$) and sodium fluorescein (filled circles; in units of ng min^{-1}) into 0.145 M NaCl solution over several hours is shown for each reservoir. The experimental procedures and release-rate calculations were the same as in Fig. 3, with the addition that samples (1 ml) were taken every several minutes from the release medium, analysed for radionuclide content in a scintillation counter, and replaced with an equal volume of fresh saline solution.

Received 25 August; accepted 16 November 1998.

1. Kost, J. & Langer, R. Responsive polymeric delivery systems. *Adv. Drug Delivery Rev.* **6**, 19–50 (1991).
2. Kwon, I. C., Bae, Y. H. & Kim, S. W. Electrically erodible polymer gel for controlled release of drugs. *Nature* **354**, 291–293 (1991).

- Bae, Y. H., Kwon, I. C. & Kim, S. W. in *Polymeric Drugs and Drug Administration* (ed. Ottenbrite, R. M.) 98–110 (Am. Chem. Soc., Washington DC, 1994).
- Miller, L. L. Electrochemically controlled release of drug ions from conducting polymers. *Mol. Cryst. Liq. Cryst.* **160**, 297–301 (1988).
- Hepel, M. & Fijalek, Z. in *Polymeric Drugs and Drug Administration* (ed. Ottenbrite, R. M.) 79–97 (Am. Chem. Soc., Washington DC, 1994).
- Edelman, E. R., Kost, J., Bobeck, H. & Langer, R. Regulation of drug release from polymer matrices by oscillating magnetic fields. *J. Biomed. Mater. Res.* **19**, 67–83 (1985).
- Kost, J. & Langer, R. in *Pulsed and Self-Regulated Drug Delivery* (ed. Kost, J.) 3–16 (CRC, Boca Raton, 1990).
- Kost, J., Leong, K. & Langer, R. Ultrasound-enhanced polymer degradation and release of incorporated substances. *Proc. Natl Acad. Sci. USA* **86**, 7663–7666 (1989).
- Mathiowitz, E. & Cohen, M. D. Polyamide microcapsules for controlled release. V. Photochemical release. *J. Membr. Sci.* **40**, 67–86 (1989).
- Fischel-Ghodsian, F., Brown, L., Mathiowitz, E., Brandenburg, D. & Langer, R. Enzymatically controlled drug delivery. *Proc. Natl Acad. Sci. USA* **85**, 2403–2406 (1988).
- Siegel, R. A., Falamarzian, M., Firestone, B. A. & Moxley, B. C. pH-controlled release from hydrophobic/polyelectrolyte copolymer hydrogels. *J. Control. Release* **8**, 179–182 (1988).
- Bae, Y. H., Okano, T., Hsueh, R. & Kim, S. W. Thermo-sensitive polymers as on-off switches for drug release. *Makromol. Chem. Rapid Commun.* **8**, 481–485 (1987).
- Hoffman, A. S., Afrassibi, A. & Dong, L. C. Thermally reversible hydrogels: II. Delivery and selective removal of substances from aqueous solutions. *J. Control. Release* **4**, 213–222 (1986).
- Okano, T., Bae, Y. H. & Kim, S. W. in *Pulsed and Self-Regulated Drug Delivery* (ed. Kost, J.) 17–45 (CRC, Boca Raton, 1990).
- Gravesen, P., Branebjerg, J. & Jensen, O. S. Microfluidics - a review. *J. Micromech. Microeng.* **3**, 168–182 (1993).
- Shoji, S. & Esashi, M. Microflow devices and systems. *J. Micromech. Microeng.* **4**, 157–171 (1994).
- Wolf, S. & Tauber, R. N. *Silicon Processing for the VLSI Era Vol. 1 Process Technology* (Lattice Sunset Beach, California, 1986).
- Jaeger, R. C. *Introduction to Microelectronic Fabrication* (Addison-Wesley, Reading, Massachusetts, 1988).
- Frankenthal, R. P. & Siconolfi, D. J. The anodic corrosion of gold in concentrated chloride solutions. *J. Electrochem. Soc.* **129**, 1192–1196 (1982).
- Merchant, B. Gold, the noble metal and the paradoxes of its toxicology. *Biologicals* **26**, 49–59 (1998).
- Jiran, E. & Thompson, C. V. Capillary instabilities in thin, continuous films. *Thin Solid Films* **208**, 23–28 (1992).
- Wu, B. M. in *Microstructural Control During Three Dimensional Printing of Polymeric Medical Devices* Thesis, 25–40 MIT (1997).

Acknowledgements. We thank A. Göpferich and M. Llabres for help in the early stages of the project, and K. Jensen, C. Thompson and R. Latanision for discussions about materials and electrochemical aspects of this project. All fabrication work was carried out at the Microsystems Technology Laboratory at MIT. This work was partially supported by the US NSF.

Correspondence and requests for materials should be addressed to R.L. (e-mail: rllanger@mit.edu).

Evidence for bromine monoxide in the free troposphere during the Arctic polar sunrise

C. T. McElroy*†, C. A. McLinden† & J. C. McConnell†‡

* Environment Canada, Downsview, Ontario, Canada, M3H 5T4

† Department of Physics & Astronomy, York University, North York, Ontario, Canada, M3J 1P3

‡ Department of Earth & Atmospheric Science, York University, North York, Ontario, Canada, M3J 1P3

During the Arctic polar springtime, dramatic ozone losses occur not only in the stratosphere but also in the underlying troposphere¹. These tropospheric ozone loss events have been observed over large areas^{2,3} in the planetary boundary layer (PBL) throughout the Arctic^{4,5}. They are associated with enhanced concentrations of halogen species^{1,6–9} and are probably caused by catalytic reactions involving bromine monoxide (BrO) and perhaps also chlorine monoxide (ClO)^{1,10–12}. The origin of the BrO, the principle species driving the ozone destruction, is thought to be the autocatalytic release of bromine from sea salt accumulated on the Arctic snow pack^{10,11,13}, followed by photolytic and heterogeneous reactions which produce and recycle the oxide^{10,11,14,15}. Satellite observations have shown the horizontal and temporal extent of large BrO enhancements in the Arctic troposphere^{16,17}, but the vertical distribution of the BrO has remained uncertain. Here we report BrO observations obtained from a high-altitude aircraft that suggest the presence of significant amounts of BrO not only in the PBL but also in the free

troposphere above it. We believe that the BrO is transported from the PBL into the free troposphere through convection over large Arctic ice leads (openings in the pack ice). The convective transport also lifts ice crystals and water droplets well above the PBL^{18,19}, thus providing surfaces for heterogeneous reactions that can recycle BrO from less-reactive forms and thereby maintain its ability to affect the chemistry of the free troposphere.

We report measurements of tropospheric BrO obtained with the composition and photodissociative flux measurement (CPFM) instrument^{20,21}, which flew on board the NASA ER-2 high-altitude research aircraft during the photochemistry of ozone loss in the arctic region in summer (POLARIS) campaign. Analysis of the CPFM measurements using differential optical absorption spectroscopy (see Methods) yields apparent column densities (ACDs), which represent the number of BrO molecules per unit area along the effective path taken by the sunlight below the aircraft as it is scattered and reflected by the surface into the CPFM instrument. The ACDs obtained during a flight on 26 April 1997 were found to be in the range of $(7–15) \times 10^{14} \text{ cm}^{-2}$. Figure 1a shows that the ACDs of BrO along the flight path, shown in Fig. 2a, vary by a factor of three. Also shown are the estimated tropospheric ACDs after the stratospheric component has been removed. Accounting for the expected upper limit of 10 parts per trillion by volume (p.p.t.v.) in the stratosphere²² results in only a 15 to 35% reduction in the total ACD. Results from other flights made on 2 May and 6 May 1997 (the latter are also shown in Fig. 1a) revealed much lower ACDs of BrO, often below the detection limit of $\sim 2 \times 10^{14} \text{ cm}^{-2}$. At present, we are unaware of any significant differences in the meteorology for these periods.

Vertical column densities (VCDs), the number of BrO molecules within a vertical column above a unit area of surface, are then extracted from the ACDs (see Methods). In the following discussion, it is assumed that the tropospheric BrO is located at various heights ranging from the surface up to a maximum height of 5 km, a height chosen on the basis of observations of plume heights over leads in Arctic sea ice^{18,19}. Figure 1b shows the VCD of BrO along the flight track and Fig. 1c shows the computed BrO mixing ratio for the different schemes investigated. Assuming that all the BrO resides within the PBL and that the PBL has a height of 1 km, VCDs of $(1–3) \times 10^{14} \text{ cm}^{-2}$ or BrO mixing ratios of 50–100 p.p.t.v. are obtained. This is a factor of 2–3 larger than the maximum BrO mixing ratio previously observed within the PBL⁶. The case where the BrO is assumed to reside above the PBL, in a uniform layer between 1 and 5 km in the troposphere, resulted in a mixing ratio of 25–30 p.p.t.v. Another scheme is a uniformly mixed layer between 0 and 5 km that yielded slightly lower mixing ratios. The final case has a BrO mixing ratio of 50 p.p.t.v. in the 0–1 km PBL, typical of what is required to destroy most of the PBL ozone within a day, if bromine chemistry alone is considered¹⁰. If the remainder of the BrO is assumed to reside in the 1–5 km altitude range, mixing ratios of ~ 10 p.p.t.v. are obtained. Figure 1d–f show that there is no significant correlation of ACDs of BrO with latitude, altitude or solar zenith angle (SZA) respectively, as observed along the flight track, including the ascent (8–20 km) and a mid-flight dive down to 15 km. This implies that the bulk of the BrO is below 8 km, the approximate height of the tropopause for this flight, and is therefore in the troposphere.

From the results shown above and given current estimates of the amount of inorganic bromine in the PBL²³, it would seem that a substantial fraction of the BrO column resides in the free troposphere. This then presents two problems: how does it get there and how is it able to remain there as BrO? An associated problem is how much ozone destruction should be expected in the free troposphere as a result of the large amounts of BrO observed.

Bromine atoms, produced by the photolysis of BrO, will rapidly react with species such as HO₂, HCHO and C₂H₂ to produce relatively inactive HBr. Hence, in the absence of heterogeneous recycling, the BrO will rapidly disappear. Using the model of Tang